PCCP

PAPER

View Article Online
View Journal | View Issue

Cite this: *Phys. Chem. Chem. Phys.*, 2015, **17**, 3832

Stress effects on the initial lithiation of crystalline silicon nanowires: reactive molecular dynamics simulations using ReaxFF

Alireza Ostadhossein,[a] Ekin D. Cubuk,[b] Georgios A. Tritsaris,[b] Efthimios Kaxiras,[b] Sulin Zhang[a] and Adri C. T. van Duin*[c]

Received 10th November 2014,
Accepted 15th December 2014

DOI: 10.1039/c4cp05198j

www.rsc.org/pccp

Silicon (Si) has been recognized as a promising anode material for the next-generation high-capacity lithium (Li)-ion batteries because of its high theoretical energy density. Recent *in situ* transmission electron microscopy (TEM) revealed that the electrochemical lithiation of crystalline Si nanowires (c-SiNWs) proceeds by the migration of the interface between the lithiated Si (Li_xSi) shell and the pristine unlithiated core, accompanied by solid-state amorphization. The underlying atomic mechanisms of Li insertion into c-Si remain poorly understood. Herein, we perform molecular dynamics (MD) simulations using the reactive force field (ReaxFF) to characterize the lithiation process of c-SiNWs. Our calculations show that ReaxFF can accurately reproduce the energy barriers of Li migration from DFT calculations in both crystalline (c-Si) and amorphous Si (a-Si). The ReaxFF-based MD simulations reveal that Li insertion into interlayer spacing between two adjacent (111) planes results in the peeling-off of the (111) facets and subsequent amorphization, in agreement with experimental observations. We find that breaking of the Si–Si bonds between (111)-bilayers requires a rather high local Li concentration, which explains the atomically sharp amorphous–crystalline interface (ACI). Our stress analysis shows that lithiation induces compressive stress at the ACI layer, causing retardation or even the stagnation of the reaction front, also in good agreement with TEM observations. Lithiation at high temperatures (*e.g.* 1200 K) shows that Li insertion into c-SiNW results in an amorphous to crystalline phase transformation at Li : Si composition of ~4.2 : 1. Our modeling results provide a comprehensive picture of the effects of reaction and diffusion-induced stress on the interfacial dynamics and mechanical degradation of SiNW anodes under chemo-mechanical lithiation.

Introduction

The ubiquitous applications of high-capacity lithium-ion batteries (LIBs), particularly in portable electronics and electric vehicles, have spurred a vigorous search for high-capacity electrode materials.[1] Among all potential anode materials, Si has been recognized as an excellent electrode for the next-generation LIBs.[2] Upon lithiation at high temperature,[2–7] Si is transformed into Li_xSi alloys with x as high as 4.4 (corresponding to a mass-specific capacity of 4200 mA h g^{-1} compared to 372 mA h g^{-1} of graphitic anodes). Due to a large surface-to-volume ratio and a shortened electron and ion transport distance, nano-sized Si anodes are particularly advantageous for their higher charging–discharging rate and efficient facile strain relaxation.[8] During lithiation, c-SiNWs undergo large volumetric expansion (~300%), leading to crack nucleation and growth, and hence capacity loss.[9–14] Recent TEM studies have revealed the atomistic mechanism of the dynamic lithiation of c-Si.[15] This study illustrated that lithiation of c-Si involves lateral movement of ledges through layer-by-layer peeling-off of the close-packed {111} atomic planes.[15] This atomic lithiation process results in highly anisotropic volume expansion, which is large along ⟨110⟩ and small along ⟨111⟩ crystallographic directions. This anisotropic swelling leads to the stress concentration and crack nucleation at the intersection of neighboring {110} planes of lithiated outer shells, as demonstrated by scanning electron microscopy (SEM) and TEM studies.[16–18]

The stress effect on the Li transport rate in c-Si and a-Si during charging and discharging processes has also been a subject of research. TEM studies revealed that the growth rate of the amorphous Li_xSi shell (the speed of the reaction front)

[a] *Department of Engineering Science and Mechanics, Pennsylvania State University, 409A EES Building, University Park, PA 16802, USA*
[b] *Department of Physics and School of Engineering and Applied Sciences, Harvard University, Cambridge, Massachusetts 02138, USA*
[c] *Department of Mechanical and Nuclear Engineering, Pennsylvania State University, University Park, PA 16802, USA. E-mail: acv13@psu.edu*

during lithiation of c-SiNWs[19] or c-SiNPs[20] decreases as lithiation proceeds. The reduced growth rate is mainly due to the slowing down of the reaction front movement since lithiation of nanostructures is reaction limited. The slowing down of the reaction front was attributed to the compressive stress at the reaction front and in the lithiated shell.[15,19–22] The time evolution of stress in electrodes during lithiation has been examined within a wide variety of electrochemical systems using the cantilever beam-bending[23–25] and the multi-beam optical sensor (MOS) technique.[26] The maximum measured stress is ~10–12 MPa for graphitic based anodes,[27] and 0.5 GPa for the amorphous layer of lithiated Si anodes.[28] These values provide important constraints for the development of reliable continuum mechanics models.

Several computational efforts have been undertaken to understand the lithiation process of c-Si, especially on the stress generation and fracture in Si. The continuum-based analytical model by Zhao *et al.*[29] accounted for the interfacial movement and plasticity in spherical nanoparticles. Pharr *et al.*[30] developed a kinetics-based model by specifying anisotropic motion of phase boundaries and simulating the corresponding morphology changes. McDowell *et al.*[20] have suggested a kinetics model to account for the effect of stress on the interface reaction rate. Yang *et al.*[31] established a model that couples Li diffusion and elasto-plasticity, which is well suited to simulate the anisotropic swelling of nanowires of different crystallographic orientations. This coupling model was recently extended by incorporating the stress effect into the lithiation kinetics.[32,33] At the atomic scale, Tritsaris *et al.*[34] performed density functional theory (DFT) calculations in conjunction with stochastic simulations to characterize lithiation kinetics in c-Si. In their work, the calculated Li migration barrier between two tetrahedral interstitial sites in c-Si is ~0.55 eV, slightly lower than that calculated by Kim *et al.*[35] and 0.58 eV calculated by Wan *et al.*[36] Tritsaris *et al.* also calculated the migration barriers pertinent to the Li insertion into a-Si for several pathways and found dissimilar values ranging from relatively low energy barriers (<0.5 eV) to barriers as high as 2.4 eV.[34]

The lithiation reaction of c-Si[37–40] and a-Si[41] has been studied extensively using first principles calculations. By modifying the algorithm proposed by Chevrier and Dahn,[42] Chan *et al.*[40] performed a series of *ab initio* simulations to rationalize the experimentally observed lithiation behaviors of c-Si. Their results showed that Li insertion into the Si(110) surface is thermodynamically more favorable than the (100) or the (111) surface. The dynamic atomic process involved in the reaction of Li and Si including stress effects has not yet been thoroughly studied, partly because of the lack of reliable interatomic potentials for Li–Si systems. In this paper, we carry out ReaxFF-based MD simulations to examine lithiation dynamics in c-SiNWs at the atomic scale. We compare the migration barriers of Li in a-Si obtained by ReaxFF with those obtained by DFT calculations to validate the Li/Si ReaxFF. We quantify the lithiation-induced stress distribution and the effect of bi-axial stress on the lithium insertion kinetics in lithiated c-SiNWs. Our results demonstrate the decisive role of local stress in the migration of the interface between lithiated and pristine Si.

Computational details

ReaxFF potential for the Si–Li system

Since the initial lithiation of c-SiNWs at room temperature involves chemical reactions and possibly fracture, the interatomic potential for MD simulations should be able to describe the bond breaking and bond formation processes accurately. The ReaxFF for Si–Li systems developed by van Duin *et al.*[43] is adequate for this purpose. ReaxFF has been successfully used for studying both anode[44,45] and cathode[46] battery materials in LIBs. Similar to non-reactive potentials, the system energy in a ReaxFF-based model is composed of several partial energy terms. The ReaxFF utilizes bond order and bond distance relations, as first introduced by Abell,[47] which can handle both bond breaking and forming by calculating the transition states of chemical reactions.[48] The total system energy is obtained by summing over several energy terms including the electron lone pairs, over-coordination, under-coordination, valence and torsion angles, conjugation, hydrogen bonding, and van der Waals and Coulomb interactions. ReaxFF determines a partial charge of individual atoms based on the electronegativity equalization method (EEM) that provides a geometry-dependent charge distribution.[49] The exact functional descriptions of each term of the ReaxFF potential are presented in detail in previous publications.[50] In the present study, we use the force field parameters by Fan *et al.*[51] The system-specific parameters contained in the ReaxFF potential were optimized against a DFT training set consisting of bulk c-Li_xSi and a-Li_xSi phases. This force field has been successfully used to determine the mechanical properties of a-Li_xSi alloys[51] as well as the diffusion of Li within c-Si. Energy barriers for diffusion of Li atoms in a-Si were not explicitly included in the training set. As a critical test of the accuracy of the ReaxFF method, we first investigated the energy barriers for diffusion of a single Li atom through a diamond cubic super-cell of 64 Si atoms, corresponding to a 2 × 2 × 2 multiple of the 8-atom diamond cubic cell. We also evaluated the ReaxFF barriers in amorphous bulk structures of Si adapted from ref. 34. In that study, the pathways for atomic Li diffusion and the corresponding energy barriers of Li migration within crystalline silicon and fourfold coordinated a-Si were obtained using DFT-based nudged elastic band (NEB) calculations. Here, we use a bond-restraint approach to find the minimum energy pathways on the potential energy surface between two sites for Li insertion that represents stable local energy minima. To explore the Li migration pathways between two equilibrium neighboring sites of the Li atom, a penalty potential function is added to the ReaxFF energy to maintain the distance between two adjacent sites using the expression

$$E_{\text{restraint}} = f_1\left(1 - e^{f_2\left(r_0 - r_{ij}\right)^2}\right)$$

In this expression, f_1 and f_2 are constants; during each MD step, the value of the distance between two sites r_{ij} is modified to sample the pathway between two local minima separated by the initial distance r_0. For the case of a single Li atom in c-Si, the thermodynamically favorable site for Li atom insertion is the tetrahedral (T_d) interstitial position at a distance of b_0 = 2.37 Å away

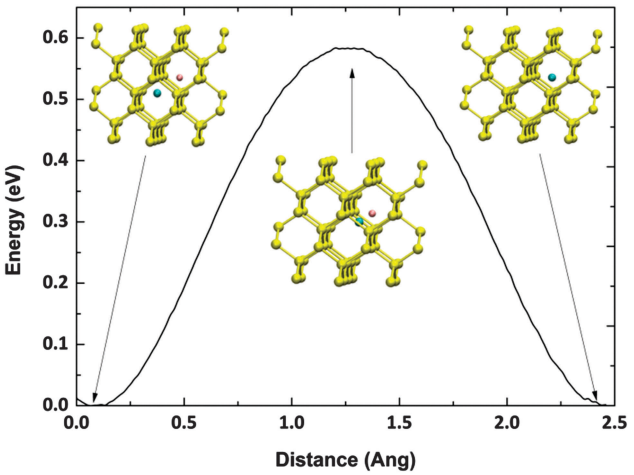

Fig. 1 Energy landscape for diffusion of one single Li-atom in c-Si from one equilibrium T_d site to an adjacent one through the hexagonal configuration (transition state). The yellow spheres represent Si atoms, the blue and pink spheres represent the Li atom in its initial, saddle-point and target (final) configuration.

from a Si atom in the direction opposite from one of its nearest neighbor Si atoms. The Li diffusion path consists of the Li migration between two adjacent T_d interstitial sites passing through the hexagonal (Hex) site. The energy landscape along the diffusion pathway as well as the initial, final and transition state of Li atoms are shown in Fig. 1. The barrier height obtained from our MD simulation is about 0.58 eV, which is in close agreement with the available DFT (0.55 eV)[35] and experimental values (0.57–0.79 eV).

The Hex site, in which there are six nearest-neighbor Si atoms with Li–Si distances of 2.37 Å, corresponds to the transition state along the diffusion pathway. We examined several values for the f_1 and f_2 constants.

For the case of Li diffusion in bulk a-Si, 3 different configurations and their corresponding energy paths from ref. 34 were chosen and their energy barriers were calculated. The comparison between the energy barriers found by ReaxFF and the corresponding DFT results is shown in Fig. 2. In these examples that involve energy barriers ranging from $\sim$0.7 eV to $\sim$2.0 eV, a Li atom moves from the first equilibrium T_d-like site, representing a local-minimum energy position surrounded by 4 Si atoms, to a neighboring one. Although the energy of Li atoms at the final configuration as estimated by ReaxFF is slightly different from the DFT results, the barrier energies are in reasonable agreement with DFT results.

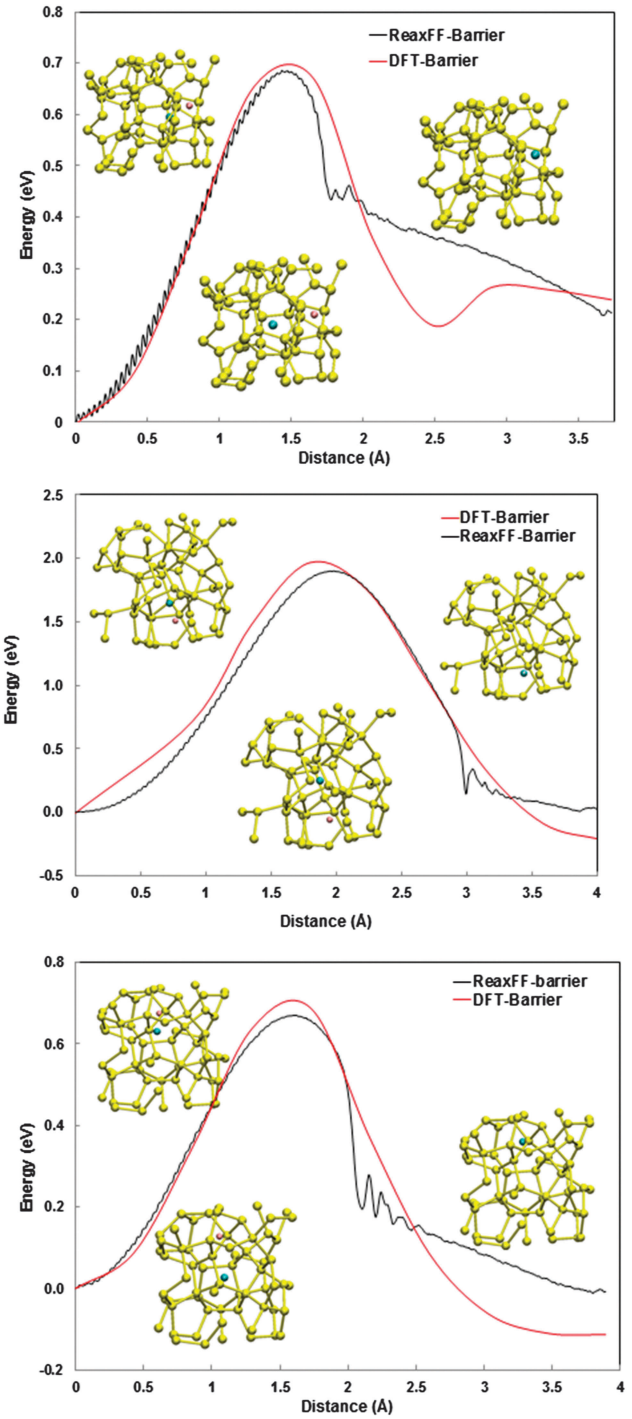

Fig. 2 Comparison between the diffusion barriers and configurational paths for Li migration within a-Si in three representative cases: DFT results (red lines) *vs.* ReaxFF results (black lines). Symbols are the same as in Fig. 1.

Reactive MD simulations using ReaxFF

MD simulations were carried out in the microcanonical ensemble using the velocity Verlet algorithm with a time step of 0.25 fs using the ReaxFF, implemented in the Large-scale Atomic/Molecular Massively Parallel Simulator (LAMMPS) package. To elucidate the lithiation process in c-SiNWs, similar to the experimental settings,[15] we constructed a ⟨112⟩-oriented c-SiNW of width 8.43 nm and height 9.22 nm, containing 5976 Si atoms. As shown in Fig. 3a, the $[\bar{1}\bar{1}1]$ surface of the nanowire is exposed to a Li reservoir consisting of a block of randomly dispersed Li atoms. Periodic boundary conditions were imposed along the x and y directions, corresponding to the [110] and [111] directions, respectively. A reflective boundary condition was applied on the top layer to keep the Li atoms from exiting the simulation box. The bottom layer is kept fixed, while the rest of the system is allowed to equilibrate. Within the *NVT* ensemble the structure is initially equilibrated at very low temperature ($\sim$1 K) using the Nosé–Hoover thermostat for 10 ps. Then the temperature was gradually

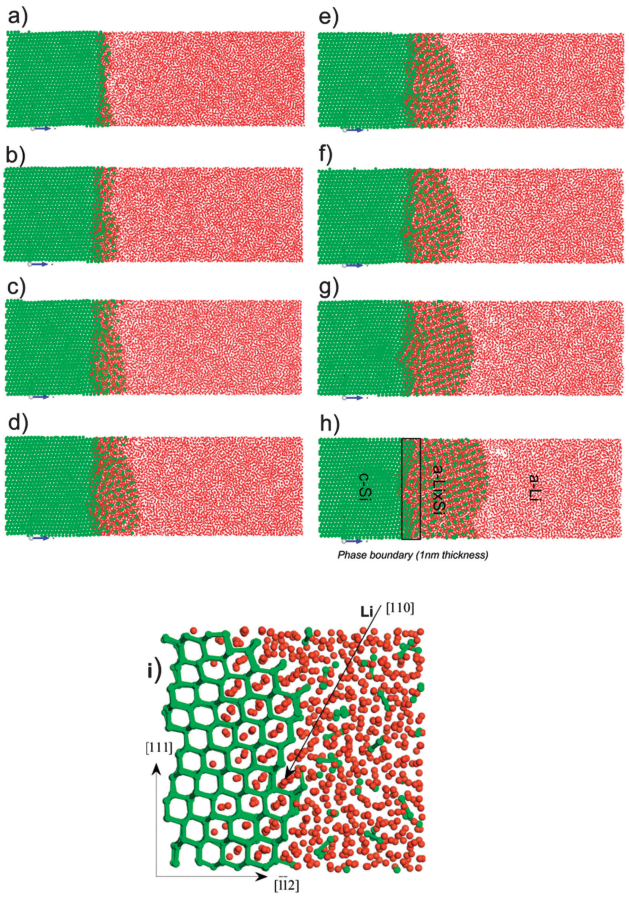

Fig. 3 Atomistic mechanism of the phase boundary evolution during initial lithiation of c-SiNW: (a–h) the movement of the amorphous–crystalline interface, which mimics the peeling-off process observed in experiment.[15] The layer-by-layer peeling-off mechanism (Layer 1 in (a) to Layer 8 in (h)) drives the solid-state amorphization by a ledge-flow. The reaction-front is highlighted by the rectangular region within the black line in (h). (i) Close up view of the mechanism of solid-state amorphization near the edge of {111} facets: the Si–Si bonds break when Li atoms diffuse preferentially in the [110] direction.

increased to 600 K with a rate of 0.048 K fs^{-1}. The system was subsequently equilibrated at 600 K at the end of simulation ($\sim$2.2 ns). The structures at successive stages of lithiation were analysed using the radial distribution function (RDF), defined as the probability of finding a particle in the distance r from a central particle:

$$g(r) = \frac{n(r)}{4\pi r^2 \rho \Delta r} \quad (1)$$

where $n(r)$ is the number of atoms located inside a shell within the region of $r \pm \Delta r/2$. Here, Δr denotes the thickness and $\rho = V/N$ is the bulk number density in which N represents the number of particles in the model volume V. Using the RDF the number of atoms located in the first coordination shell, referred to as the first coordination number CN, is obtained as:

$$\mathrm{CN} = \int_0^{r_1} \rho \cdot 4\pi r^2 g(r) \mathrm{d}r$$

where r_1 is the first minimum in the $g(r)$ curve. In the present study we use CN to find the number of four-fold coordinated Si-atoms in the crystal nanowire region. Based on the calculated RDF of c-SiNW, the first, second, third and fourth nearest neighbors of Si atoms are located on average at 0.23 nm, 0.38 nm, 0.44 nm, and 0.53 nm, respectively, which are close to both DFT and experimental values for c-SiNWs.[52] The RDFs pertinent to the lithiation steps are obtained by extracting configurations at 0.15 ps intervals from the MD trajectories between 6 and 30 ps after the system has reached equilibrium.

Stress evaluation

The stress calculations are based on the definition of virial stress:

$$\boldsymbol{\sigma}_{\mathrm{virial}} = \frac{1}{\Omega}\left(-m_i \dot{\mathbf{u}}_i \otimes \dot{\mathbf{u}}_i + \frac{1}{2}\sum_{j \neq i} \mathbf{r}_{ij} \otimes \mathbf{f}_{ij}\right) \quad (2)$$

with Ω the atomic volume of particle i, $\mathbf{r}_i - \mathbf{r}_i^0$ is the displacement of atom i with respect to its reference position, $\mathbf{r}_{ij} = \mathbf{r}_i - \mathbf{r}_j$ is the distance between atoms labeled i and j, and $\mathbf{f}_{ij}$ is the force on atom i. The virial stress can generally be interpreted in a volume and time average sense, according to derivation given in ref. 53. We calculated the stress as the symmetrized per-atom stress tensor. The stress distribution will be used to study the influence of pressure on the reaction of Li and Si during insertion of lithium atoms into SiNW anodes of LIBs.

Results and discussion

Degradation of c-SiNW during lithium insertion

To model the mechanism of solid-state amorphization, we performed a series of MD simulations at elevated temperatures in order to speed up the Li diffusion in Si. During the amorphization process, the negative heat of formation of Li_xSi phases causes the Li atoms to move into the pristine Si{111} surface along the ⟨110⟩ direction, and accumulate locally near the Li/Si interface by forming the first lithiated layer. In the present study, motivated by previous DFT studies through which the amorphous Li–Si structures were thermalized at high temperature (900–1500 K),[54,55] we employ a temperature ranging from 600–1200 K. Fig. 3a–h display the morphological evolution of c-SiNW upon Li insertion. These results can be directly compared to the high-resolution TEM images reported in ref. 15. As seen in Fig. 3a, Li prefers to occupy the first available tetrahedral sites (T_d) in the first sub-layer and lithiation proceeds by the simultaneous lateral ledge flow of silicon (indicated by colored arrows) at the interface layer and peeling-off of {111} planes. Fig. 3a–h clearly demonstrate that the [110] direction is the primary channel for Li diffusion. The atomically resolved lithiation dynamics shown in Fig. 3a–h agree with the high resolution TEM studies (Fig. 2 of ref. 15). Additional Li insertion occurs when Li atoms occupy the remaining tetrahedral (T_d) sites between two adjacent ($\bar{1}\bar{1}1$) planes consecutively and breaks the Si–Si bonds lying on the zigzag-like ($\bar{1}\bar{1}1$) sites. Each monolayer of the {111} surfaces is lifted-off when all four possible T_d sites below the surface are occupied and all the Si–Si covalent bonds between the two bilayers, the one forming the

surface and the one directly below it, break. Dissolution of the dissociated c-Si layers through the addition of Li leads to an amorphous layer of Li_xSi separated by a thin layer of lithiated Si, forming the so-called amorphous crystalline interface (ACI).

The ACI-layer has a thickness of about 1 nm. The thickness does not change as the reaction front propagates. This observation is consistent with previous DFT[37] and experimental[15] studies. As will be discussed later, the development of the ACI layer that starts with disintegrating of silicine-like {111} sheets from the surface of the nanowire proceeds by breaking down these planar structures into zigzag chains and isolated Si atoms at higher concentration of Li. To elucidate the structural evolution of the Si network upon lithiation, we compare in Fig. 4 the radial pair distribution functions $g_{Si-X}(r)$ (with X = Si in Fig. 4a and X = Li in Fig. 4b), corresponding to the successive steps (Layer 1 to Layer 8) of peeling-off of c-Si. As seen from this figure, during the lithiation procedure, the total number of Si–Si neighbors decreases, while the number of Li–Si neighbors increases. The sharp peaks in the $g(r)$, especially those associated with the second and third nearest neighbors, diminish due to the disruption in the initial c-Si structure. The loss of crystalline order and the formation of the amorphous layer of lithiated Si are indicated by lower and broader peaks. Moreover, the shifting of the peaks to larger Si–Si bond length indicates the occurrence of a phase transformation within the reaction front.

The electrochemical lithiation of c-Si at room temperature results in the formation of metastable a-Li_xSi phases, with a Li : Si ratio of $x \approx 3.75$. The transformation of c-Si into c-Li_xSi is only observed at high temperature. As depicted by Fig. 5a and b, the progressive Li migration into the c-Si at T = 1200 K, and simultaneous growth of the a-Li_xSi shell trigger the formation of an ordered phase in the middle of the lithiated amorphous layer. Comparison between the partial RDFs pertinent to the a-Li_xSi layers behind the reaction-front (Fig. 5b) and those obtained from bulk c-$Li_{15}Si_4$ phases (reported in Fig. 4 of ref. 56) illustrates the atomic similarities between these crystalline-like regions and the c-$Li_{15}Si_4$ structures. Specifically, the peaks of radial distribution function of the Si–Si bond are located at the same position of peaks in $Li_{15}Si_4$ reported in ref. 56. This comparison reveals the crystallization of a-$Li_{15}Si_4$ in our MD simulation at high temperature and high Li content. To gain a better understanding of the structural features and the composition of the various compounds during ACI formation, we evaluate the statistics of Si-rings during lithiation. The ring counting method has been used to describe medium-range order in amorphous materials (see, for example, ref. 41 and 57).

We choose the value of $r \leq 2.5$ Å as a representative cutoff radius for identifying nearest neighbors, which corresponds to the first coordination shell of Si in the crystalline phase. Before lithiation, in the pristine Si lattice, the fourfold coordinated Si atoms form only 6- and 8-membered rings; as lithiation progresses, these rings gradually break down to smaller 5- and 7-membered rings, consisting of 5- and 7-atom chains, and dissolve into the already lithiated amorphous layer. Due to the continuous breaking of the covalent Si–Si bonds, during lithiation the number of 6- and 8-membered rings per Si atom diminishes from an initial value of 3 in pure Si to 0.09 at 600 K and to 0.04 at 900 K. The number of 6- or 8-membered rings settles to almost constant values (the lower ones mentioned) after 30 ps. We also find that at higher temperatures (1200 K), the probability

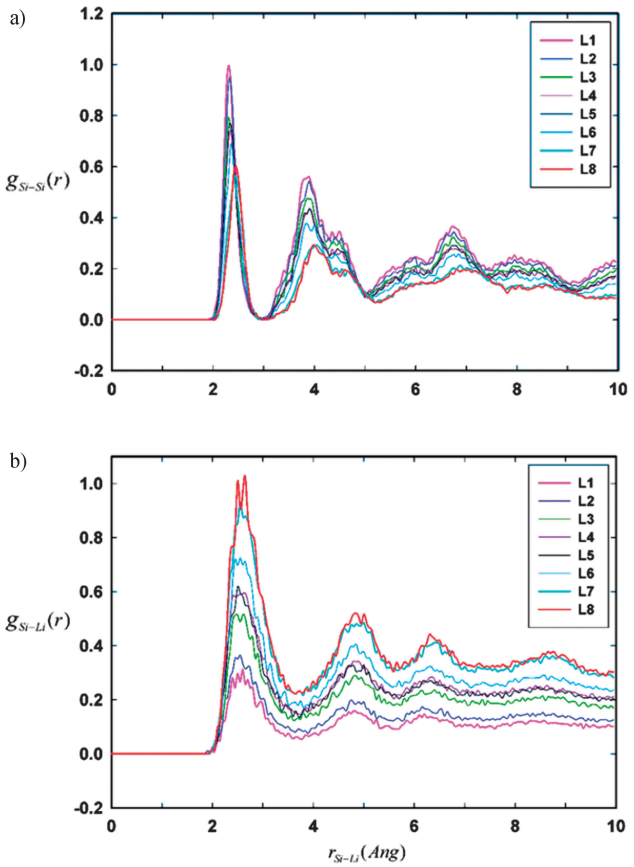

Fig. 4 Radial pair distribution function $g(r)$ at 600 K for Si–Si and Si–Li during different stages of solid-state amorphization: 1 to 8 signifies the number of Si-layers peeled-off from the c-SiNW under lithiation.

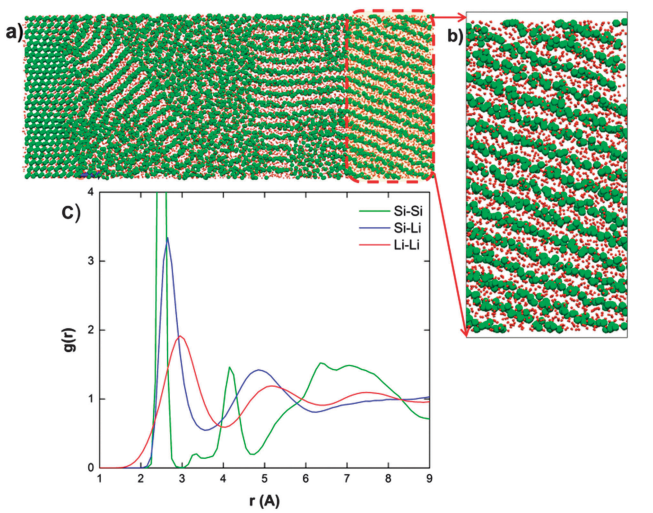

Fig. 5 (a) and (b) Atomic configurations, and (c) radial pair distribution function $g(r)$ at 1200 K for Si–Si and Li–Si/Li. These results reveal the crystallization of Li_xSi at high Li concentration ($x \approx 4.2$).

of formation of 3- and 4-membered Si rings grows. The Si–Si bond weakening and breaking lead to formation of 5- and 7-membered rings which was also reported in previous DFT studies.[41,55]

Stress evolution during lithiation

When Li atoms diffuse into the host Si crystal and react, a compressive stress is produced near the interface. Furthermore, the reaction between Li atoms and intact portions of the c-Si lattice induces the host atoms to flow into the already lithiated phase. The concurrent reactive flow in solids is commonly observed throughout a number of chemical processes such as inelastic deformation of cement[58] and formation and growth of oxide layers upon metal oxidation.[59] As shown in a previous section, Li–Si reactions form a sharp interface that separates the crystalline core and the lithiated shell. The nearly lithiated products at the reaction front push previously lithiated layers outward by reactive flow and large deformation. Zhao *et al.*[60] have shown that reactive flow in a Si anode is assisted by Li incorporation in breaking and reforming the Si–Si bonds. Here, we calculate the stress distribution in the c-SiNW during the lithiation process. To achieve this, a symmetric stress tensor was calculated for each atom using eqn (2) and its components were averaged over a length of 2.40 Å, which corresponds to the Si–Si first coordination shell in the reference Si configuration. Fig. 6 displays the evolution of diffusion induced hydrostatics mean stress, $\sigma_m = \frac{\sigma_{11} + \sigma_{22} + \sigma_{33}}{3}$ and von-Mises stress $\sigma_v = \sqrt{\frac{3}{2} s_{ij} s_{ij}}$, where $s_{ij} = \sigma_{ij} - \sigma_m \delta_{ij}$ is the deviatoric tensor in the c-SiNW during the Li insertion. Here δ_{ij} is the Kronecker delta. Compressive hydrostatic stress hinders the Li reaction and diffusion while tensile stress enhances them in the c-SiNW. Recent *in situ* TEM by McDowell *et al.*[20] examined the lithiation of a group of silicon nanoparticles (SiNPs) with various sizes and found that, regardless of the NP size, the lithiation rate slows down on similar time scales. They concluded from their experiments that the kinetics of the Li reaction during lithiation of SiNPs is controlled by the interface reaction rate instead of Li diffusion through the Li_xSi shell. To interpret their results, following Zhao *et al.*,[60] they argued that the crystalline core experiences homogeneous hydrostatic compression, applied by the previously lithiated Li_xSi shell, which increases when the core size decreases. This increasing hydrostatic pressure progressively slows down the electrochemical reaction at the reaction front. As depicted in Fig. 6 the hydrostatic stress is compressive throughout the entire simulation and its absolute value increases gradually as lithiation proceeds. The stress field in the a-Li_xSi shell, however, is inhomogeneous. The stress field obtained from our MD simulations is in the range of stresses reported by both continuum scale simulations (see ref. 21) and experiments. Since the Li insertion-induced pressure is relatively low in the early stage of simulation, the growth of the lithiated layer and the diffusion of Li atoms within the c-SiNW are much faster in the initial stages. The growing pressure can reduce the driving force for reaction and eventually can suppress it, and consequently lithiation comes to a complete stop. Up to 30 ps, Li does not alter the Si network markedly; further lithiation will rearrange the initial crystal structure through the Si–Si bond breaking and bond forming. Results of our MD simulations at T = 600 K demonstrate that the compressive hydrostatic stress, induced by Li diffusion into Si, imposes a self-limitation on the lithiation process so that it stops the Li insertion at pressures

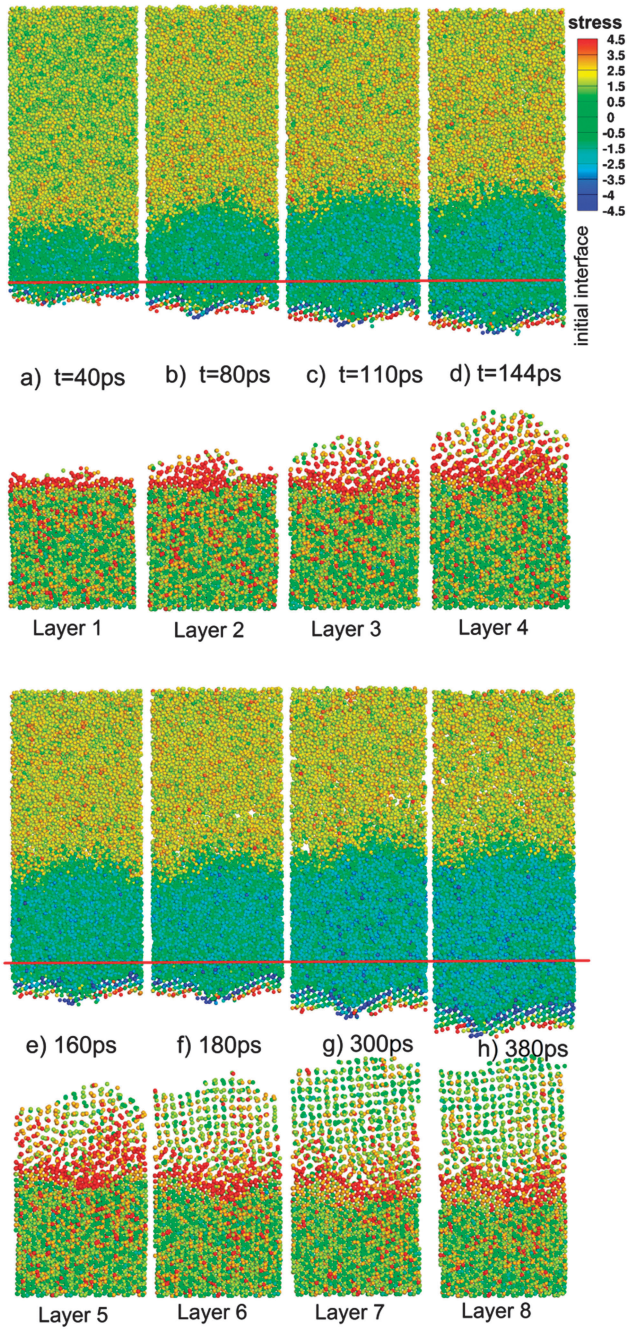

Fig. 6 Stress distribution during the lithiation of c-SiNW at T = 600 K. The snapshots correspond to the successive steps of peeling-off shown in Fig. 3a–h. The top inset is the hydrostatic stress distribution induced by Li insertion into the c-SiNW. The bottom row shows the von Mises stress in the Si(111) atomic layers. The red line is the original interface before the simulation starts. The atoms are colored on the basis of their virial stresses, shown in the color bar.

higher than 4.5 GPa. This onset of lithiation retardation has not been previously reported neither by experiments nor by simulations. The distribution of von-Mises stress (bottom set in Fig. 6a–h) shows the atomic {111} planes which were peeled-off from the original c-SiNW and undergo plastic deformation. Moreover, this stress diminishes very fast when the detached layers break down to smaller clusters and single isolated atoms spreading out within the previously lithiated shell.

The concentration profile reveals that the average Li-concentration of the amorphous lithiated layers beyond the reaction front is about 4.3, which is in close agreement with the values reported in experimental studies about the lithiation of c-Si at high temperature.[3–6] Apart from the structural resemblance of the lithiated configurations at 1200 K with the c-$Li_{15}Si_4$ configurations, highlighted in Section 3, the obtained concentration can be inferred as evidence for the crystallization of Li rich phases in our simulations. Herein, we performed a bond count using a bond order cut-off equal to 0.3 in order to identify the bond dissociation and bond formation process during our reactive MD simulations. Based on this bond order cut-off, the distribution of Si–Si and Li–Si bonds across the simulation box was obtained and plotted as a function of time in Fig. 7a and b respectively.

The number of fourfold coordinated Si atoms decreases from initial 5470 atoms to 4870 and then becomes constant as lithiation progresses, as indicated in Fig. 7b. Since the number of Si–Li bonds does not change significantly after 400 ps, here we only report the results prior to this stage in our simulations.

Effect of bi-axial compressive stress on the mechanism of c-SiNW degradation

Since diffusion and reaction both play an important role in the formation of the ACI layer, achieving a detailed understanding of the stress-mediated lithiation rate can provide guidance to the rational design of the SiNW anodes. Johari *et al.*[55] reported that the pressure induced on the side walls of the simulation box during the mixing of Li and Si atoms and during the formation of Li_xSi amorphous phase changes from 1.5 GPa at 900 K to 3 GPa at 1200 K. This huge amount of stress affects the phase boundary evolution during the insertion of Li atoms into c-SiNWs. To examine the influence of compressive stress, a c-SiNW with a {110}-orientation was considered under applied biaxial compressive stress along the x and y directions. The Si(110) facet was chosen since the reaction front motion is faster along the ⟨110⟩ direction. The periodic cell dimensions are allowed to vary in the planar directions, that is, x-⟨001⟩ and y-⟨1$\bar{1}$0⟩, by using a Berendsen barostat, but are kept constant in the z direction. In this section, the simulations were performed on a model consisting of 3839 Si and 3839 Li atoms arranged in a 6.56 nm × 1.55 nm × 15.49 nm simulation box. Following the same procedure described in Section 2, the system was equilibrated at 1 K prior to heating up to 600 K using a Berendsen thermostat with a 0.1 ps damping ratio under an *NPT* ensemble while the pressure on two sides of the c-SiNW was kept constant to the desired values ranging from 1 GPa to 3 GPa.

Fig. 8 shows the time variation in the thickness of the (110)-ACI layer and the number of Li atoms below the original interface of Si and Li. Fig. 8a indicates that by increasing the confining pressure,

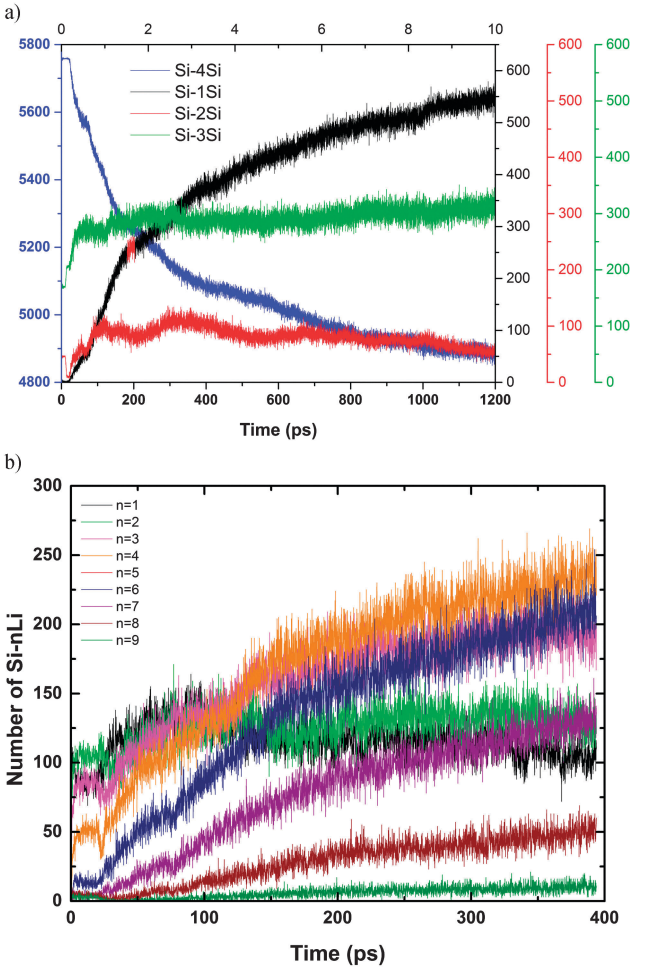

Fig. 7 Variation of the coordination number of Si–Si (a) and Si–Li (b) bonds during the lithiation of (112) c-SiNW at 600 K. The thickness of lithiated layer increases linearly but exponentially decays after 0.2 ns.

P_x and P_y, the Li atoms diffuse slower toward the c-SiNW. Moreover, the rate of solid-state amorphization, which can be interpreted as the velocity of the phase boundary as obtained from the slope of the curves in Fig. 8b, decreases compared to the fast rate of growth at the early stages of lithiation. The evolution of the reaction front suggests that the kinetics of reaction is initially controlled by the interface, resulting in linear growth of the lithiated layer and switches to the diffusion controlled regime after $t \approx 250$ ps. Since each Li atom is presumed to react with the intact crystalline Si-layer due to its chemical potential, the bi-axial pressure acting on the side walls of nanowire affects the kinetics of the reaction by changing the chemo-mechanical driving forces for insertion of the Li atoms. Similar to the case of the ⟨112⟩ oriented c-SiNW, the lifted top layers are assimilated into the a-Li_xSi phase and do not affect the progression of the reaction front. Additionally, time-evolution of the breaking Si–Si bonds and formation of Li–Si bonds, denoted by the variation of coordination-numbers associated with Si atoms in Si–Si and Si–Li pairs, shows that while the number of four-fold coordinated Si atoms gradually decreases, the Si^{n+} components, which bind to n = 1–9 nearest vicinal Li atoms, increase as the lithiation progresses. The growth of the lithiated (Si^{1+-9+}) layer

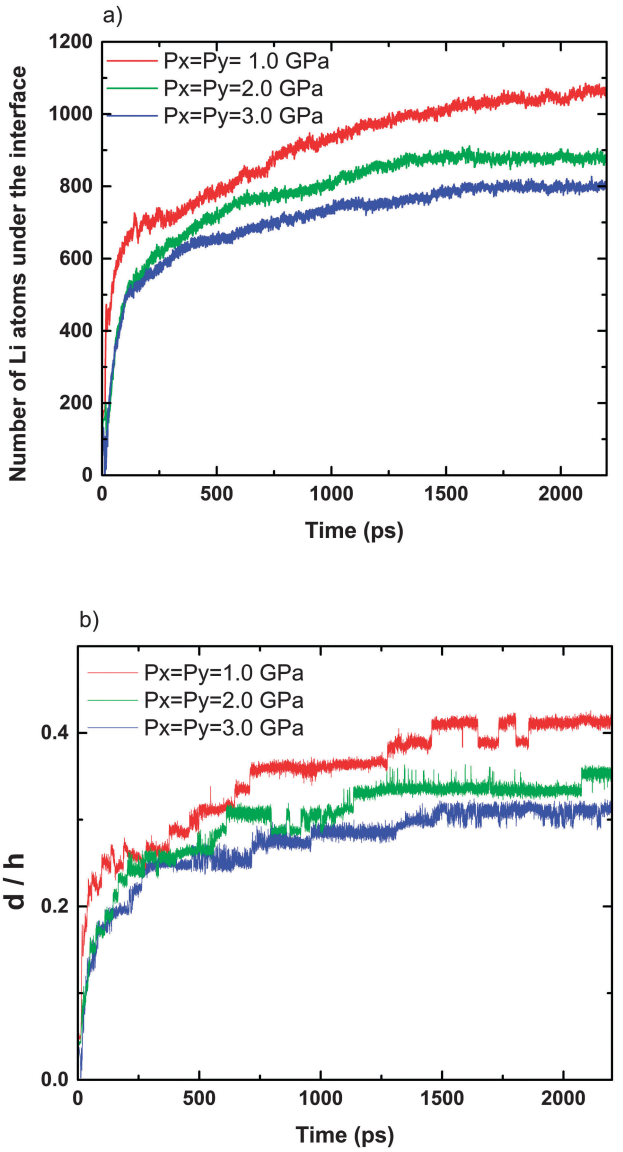

Fig. 8 The variation of the lithiation rate of Si(110) nanowires as a function of simulation time and the formation of lithiated layers as a function of bi-axial pressure on the Si-NW. (a) The numbers of Li atoms penetrating below the original interface. (b) The time evolution of reaction front movement at different prescribed pressure levels. The distance is normalized with respect to the initial c-SiNW height (h).

initiates linearly at the beginning, but stops after 160 ps due to the retardation effect of lithiation-induced pressure. Our results quantitatively show that the lithiation process is strongly influenced by the decrease of the thermodynamic driving force for lithiation related to the bi-axial pressure on the side-walls of the c-SiNW.

Conclusions

In this work we presented large-scale MD simulations using the ReaxFF potential to study Li insertion into c-SiNWs in LIBs. A comparison of barrier energies obtained by ReaxFF and DFT simulations demonstrates the transferability of the potential to predict the Li-diffusion behavior in both crystalline and amorphous phases of the Si network. Our reactive MD simulations at elevated temperatures (T = 600 K, 1200 K) on a ⟨112⟩ c-SiNW reveal that the lithiation of c-Si proceeds by a layer-by-layer peeling-off of pristine Si layers, and features an atomically sharp interface that separates the lithiated amorphous shell and the unlithiated crystalline core. The obtained morphology of the ACI layer is in good agreement with previously reported high resolution TEM images.[15] The interlayer Si–Si bonds (between {111} bi-layers) break only when several Li atoms concentrate in the vicinity of the bond. We quantified the hydrostatic stress induced by Li diffusion as well as the von Mises stresses acting on the Si-layers upon lithiation and found that these stresses slow down the lithiation process. According to our findings, a hydrostatic pressure higher than 4.5 GPa leads to a complete stop of lithiation. Our modeling results can shed light on the chemo-mechanical insertion process of Li into the new high-capacity Si negative electrodes and provide fundamental guidance to the rational designs of the next generation high capacity electrode materials with enhanced capacity retention and durability.

Acknowledgements

AO and ACTvD acknowledge the support of the Fluid Interface Reactions, Structures and Transport (FIRST) Center, an Energy Frontier Research Center funded by the U.S. Department of Energy, Office of Science, and Office of Basic Energy Sciences, for the Li/Si ReaxFF parameter development. ACTvD and EK acknowledge support from a grant from the U.S. Army Research Laboratory through the Collaborative Research Alliance (CRA) for Multi Scale Multidisciplinary Modeling of Electronic Materials (MSME) for DFT-calculations on amorphous Li/Si materials and for ReaxFF MD-simulations.

References

1 X. Yuan, H. Liu and J. Zhang, *Lithium-ion batteries: advanced materials and technologies*, CRC Press, 2011.
2 U. Kasavajjula, C. Wang and A. J. Appleby, *J. Power Sources*, 2007, **163**, 1003–1039.
3 R. A. Sharma and R. N. Seefurth, *J. Electrochem. Soc.*, 1976, **123**, 1763–1768.
4 B. A. Boukamp, G. C. Lesh and R. A. Huggins, *J. Electrochem. Soc.*, 1981, **128**, 725–729.
5 C. J. Wen and R. A. Huggins, *J. Solid State Chem.*, 1981, **37**, 271–278.
6 C. Van der Marel, G. J. B. Vinke and W. Van der Lugt, *Solid State Commun.*, 1985, **54**, 917–919.
7 J. Rohrer and K. Albe, *J. Phys. Chem. C*, 2013, **117**, 18796–18803.
8 K. T. Lee and J. Cho, *Nano Today*, 2011, **6**, 28–41.
9 L. Y. Beaulieu, K. W. Eberman, R. L. Turner, L. J. Krause and J. R. Dahn, *Electrochem. Solid-State Lett.*, 2001, **4**, A137–A140.

10 L.-F. Cui, R. Ruffo, C. K. Chan, H. Peng and Y. Cui, *Nano Lett.*, 2008, **9**, 491–495.
11 C. K. Chan, H. Peng, G. Liu, K. McIlwrath, X. F. Zhang, R. A. Huggins and Y. Cui, *Nat. Nanotechnol.*, 2007, **3**, 31–35.
12 B. Hertzberg, A. Alexeev and G. Yushin, *J. Am. Chem. Soc.*, 2010, **132**, 8548–8549.
13 H. Li, X. Huang, L. Chen, Z. Wu and Y. Liang, *Electrochem. Solid-State Lett.*, 1999, **2**, 547–549.
14 M. Yamada, A. Ueda, K. Matsumoto and T. Ohzuku, *J. Electrochem. Soc.*, 2011, **158**, A417–A421.
15 X. H. Liu, J. W. Wang, S. Huang, F. Fan, X. Huang, Y. Liu, S. Krylyuk, J. Yoo, S. A. Dayeh and A. V. Davydov, *Nat. Nanotechnol.*, 2012, **7**, 749–756.
16 X. H. Liu, L. Zhong, S. Huang, S. X. Mao, T. Zhu and J. Y. Huang, *ACS Nano*, 2012, **6**, 1522–1531.
17 W. Liang, H. Yang, F. Fan, Y. Liu, X. H. Liu, J. Y. Huang, T. Zhu and S. Zhang, *ACS Nano*, 2013, **7**, 3427–3433.
18 S. W. Lee, M. T. McDowell, L. A. Berla, W. D. Nix and Y. Cui, *Proc. Natl. Acad. Sci. U. S. A.*, 2012, **109**, 4080–4085.
19 X. H. Liu, F. Fan, H. Yang, S. Zhang, J. Y. Huang and T. Zhu, *ACS Nano*, 2013, **7**, 1495–1503.
20 M. T. McDowell, S. W. Lee, C. Wang, W. D. Nix and Y. Cui, *Adv. Mater.*, 2012, **24**, 6034–6041.
21 X. H. Liu, H. Zheng, L. Zhong, S. Huang, K. Karki, L. Q. Zhang, Y. Liu, A. Kushima, W. T. Liang and J. W. Wang, *Nano Lett.*, 2011, **11**, 3312–3318.
22 S. W. Lee, M. T. McDowell, J. W. Choi and Y. Cui, *Nano Lett.*, 2011, **11**, 3034–3039.
23 K. Ueno, S.-I. Pyun and M. Seo, *J. Electrochem. Soc.*, 2000, **147**, 4519–4523.
24 S.-I. Pyun, K.-H. Kim and J.-N. Han, *J. Power Sources*, 2000, **91**, 92–98.
25 J.-Y. Go and S.-I. Pyun, *J. Electrochem. Soc.*, 2003, **150**, A1037–A1043.
26 V. A. Sethuraman, M. J. Chon, M. Shimshak, V. Srinivasan and P. R. Guduru, *J. Power Sources*, 2010, **195**, 5062–5066.
27 V. A. Sethuraman, N. Van Winkle, D. P. Abraham, A. F. Bower and P. R. Guduru, *J. Power Sources*, 2012, **206**, 334–342.
28 M. J. Chon, V. A. Sethuraman, A. McCormick, V. Srinivasan and P. R. Guduru, *Phys. Rev. Lett.*, 2011, **107**, 045503.
29 K. Zhao, M. Pharr, Q. Wan, W. L. Wang, E. Kaxiras, J. J. Vlassak and Z. Suo, *J. Electrochem. Soc.*, 2012, **159**, A238–A243.
30 M. Pharr, K. Zhao, X. Wang, Z. Suo and J. J. Vlassak, *Nano Lett.*, 2012, **12**, 5039–5047.
31 H. Yang, S. Huang, X. Huang, F. Fan, W. Liang, X. H. Liu, L.-Q. Chen, J. Y. Huang, J. Li and T. Zhu, *Nano Lett.*, 2012, **12**, 1953–1958.
32 H. Yang, F. Fan, W. Liang, X. Guo, T. Zhu and S. Zhang, *J. Mech. Phys. Solids*, 2014, **70**, 349–361.
33 M. Gu, H. Yang, D. E. Perea, J.-G. Zhang, S. Zhang and C.-M. Wang, *Nano Lett.*, 2014, **14**, 4622–4627.
34 G. A. Tritsaris, K. Zhao, O. U. Okeke and E. Kaxiras, *J. Phys. Chem. C*, 2012, **116**, 22212–22216.
35 H. Kim, K. E. Kweon, C.-Y. Chou, J. G. Ekerdt and G. S. Hwang, *J. Phys. Chem. C*, 2010, **114**, 17942–17946.
36 W. Wan, Q. Zhang, Y. Cui and E. Wang, *J. Phys.: Condens. Matter*, 2010, **22**, 415501.
37 E. D. Cubuk, W. L. Wang, K. Zhao, J. J. Vlassak, Z. Suo and E. Kaxiras, *Nano Lett.*, 2013, **13**, 2011–2015.
38 K. Zhao, W. L. Wang, J. Gregoire, M. Pharr, Z. Suo, J. J. Vlassak and E. Kaxiras, *Nano Lett.*, 2011, **11**, 2962–2967.
39 S. C. Jung, J. W. Choi and Y.-K. Han, *Nano Lett.*, 2012, **12**, 5342–5347.
40 M. K. Chan, C. Wolverton and J. P. Greeley, *J. Am. Chem. Soc.*, 2012, **134**, 14362–14374.
41 E. D. Cubuk and E. Kaxiras, *Nano Lett.*, 2014, **14**, 4065–4070.
42 V. L. Chevrier and J. R. Dahn, *J. Electrochem. Soc.*, 2009, **156**, A454–A458.
43 A. C. van Duin, S. Dasgupta, F. Lorant and W. A. Goddard, *J. Phys. Chem. A*, 2001, **105**, 9396–9409.
44 X. Huang, H. Yang, W. Liang, M. Raju, M. Terrones, V. H. Crespi, A. C. van Duin and S. Zhang, *Appl. Phys. Lett.*, 2013, **103**, 153901.
45 H. Yang, X. Huang, W. Liang, A. C. Van Duin, M. Raju and S. Zhang, *Chem. Phys. Lett.*, 2013, **563**, 58–62.
46 M. M. Islam, A. Ostadhossein, O. Borodin, A. T. Yeates, W. W. Tipton, R. G. Hennig, N. Kumar and A. C. T. van Duin, *Phys. Chem. Chem. Phys.*, 2014, DOI: 10.1039/C4CP04532G.
47 G. C. Abell, *Phys. Rev. B: Condens. Matter Mater. Phys.*, 1985, **31**, 6184.
48 T. Liang, Y. K. Shin, Y.-T. Cheng, D. E. Yilmaz, K. G. Vishnu, O. Verners, C. Zou, S. R. Phillpot, S. B. Sinnott and A. C. van Duin, *Annu. Rev. Mater. Res.*, 2013, **43**, 109–129.
49 U. Khalilov, G. Pourtois, A. van Duin and E. C. Neyts, *Chem. Mater.*, 2012, **24**, 2141–2147.
50 K. Chenoweth, A. C. van Duin and W. A. Goddard, *J. Phys. Chem. A*, 2008, **112**, 1040–1053.
51 F. Fan, S. Huang, H. Yang, M. Raju, D. Datta, V. B. Shenoy, A. C. Van Duin, S. Zhang and T. Zhu, *Modell. Simul. Mater. Sci. Eng.*, 2013, **21**, 074002.
52 D. D. D. Ma, C. S. Lee, F. C. K. Au, S. Y. Tong and S. T. Lee, *Science*, 2003, **299**, 1874–1877.
53 O. H. Nielsen and R. M. Martin, *Phys. Rev. Lett.*, 1983, **50**, 697.
54 H. Kim, C.-Y. Chou, J. G. Ekerdt and G. S. Hwang, *J. Phys. Chem. C*, 2011, **115**, 2514–2521.
55 P. Johari, Y. Qi and V. B. Shenoy, *Nano Lett.*, 2011, **11**, 5494–5500.
56 B. Key, M. Morcrette, J.-M. Tarascon and C. P. Grey, *J. Am. Chem. Soc.*, 2010, **133**, 503–512.
57 D. S. Franzblau, *Phys. Rev. B: Condens. Matter Mater. Phys.*, 1991, **44**, 4925.
58 F.-J. Ulm, O. Coussy, L. Kefei and C. Larive, *J. Eng. Mech.*, 2000, **126**, 233–242.
59 V. K. Tolpygo and D. R. Clarke, *Acta Mater.*, 2004, **52**, 5115–5127.
60 K. Zhao, G. A. Tritsaris, M. Pharr, W. L. Wang, O. Okeke, Z. Suo, J. J. Vlassak and E. Kaxiras, *Nano Lett.*, 2012, **12**, 4397–4403.

